JOURNAL OF THERMOPHYSICS AND HEAT TRANSFER
Vol. 23, No. 4, October–December 2009

# Numerical Simulation of Developing Compressible Turbulent Flow with Heat Transfer

A. Nouri-Borujerdi* and M. Ziaei-Rad†
*Sharif University of Technology, 11365-9567 Tehran, Iran*
and
J. R. Seume‡
*Leibniz University Hannover, 30167 Hannover, Germany*

DOI: 10.2514/1.41669

**This study investigates the effects of wall heating and skin friction on the characteristics of a compressible turbulent flow in developing and developed regions of a pipe. The numerical solution is performed by finite-element-based finite volume method applied on unstructured grids. A modified $\kappa$-$\varepsilon$ model with a two-layer equation for the near-wall region and a compressibility correction are used to predict turbulent viscosity. The results show that shear stress in fully developed flow is nearly constant from the centerline up to 75% of the pipe radius, then increases sharply next to the wall, and the ratio of the turbulent viscosity to the molecular one is less than 0.2. Under a uniform wall heat flux condition, the friction factor decreases in the entrance region and will be fully developed after $Z/D > 50$, but the Nusselt number increases first and then will be fully developed after $Z/D > 10$. In addition, the heat flux accelerates the developing compressible flow and causes the entrance length to decrease, unlike the incompressible flow.**

## Nomenclature

| | | |
|---|---|---|
| $A$ | = | hexagonal area, $m^2$ |
| $A$ | = | Jacobian matrix |
| $b$ | = | energy flux by force and heat, $W/m^2$ |
| $C$ | = | triangle area, $m^2$ |
| $c$ | = | speed of sound, m/s |
| $C$ | = | constant |
| $D$ | = | pipe diameter, m |
| $D$ | = | destruction, 1/s |
| $e$ | = | internal energy, J/kg |
| $F$ | = | inviscid vector flux |
| $f$ | = | friction factor |
| $H$ | = | total enthalpy, J/kg |
| $H$ | = | Heaviside step function |
| $k$ | = | thermal conductivity, $W/m \cdot K$ |
| $L$ | = | pipe length, m |
| $l$ | = | length scale, m |
| $M$ | = | Mach number ($u/\sqrt{\gamma RT}$) |
| $N$ | = | viscous flux vector, number of grid nodes |
| $Nu$ | = | Nusselt number ($hD/k$) |
| $n$ | = | unit normal vector |
| $P$ | = | production |
| $p$ | = | pressure, Pa |
| $Pr$ | = | Prandtl number ($\mu C_p/k$) |
| $Q$ | = | conservative variables vector |
| $q''$ | = | heat flux rate, $W/m^2$ |
| $R$ | = | pipe radius, m |
| $R$ | = | eigenvector matrix |
| $Re$ | = | Reynolds number ($\rho \bar{u} D/\mu$) |
| $r$ | = | radial direction |
| $S$ | = | source vector, $W/m^3$ |
| $T$ | = | temperature, K |
| $t$ | = | time, s |
| $u$ | = | velocity in the $z$ direction, m/s |
| $V$ | = | velocity vector, m/s |
| $y$ | = | distance measured from wall inward, m |
| $z$ | = | axial direction |
| $\gamma$ | = | specific heat ratio |
| $\Delta$ | = | difference |
| $\delta$ | = | boundary-layer thickness, m |
| $\varepsilon$ | = | turbulent dissipation energy, W/kg |
| $\kappa$ | = | turbulent kinetic energy, $m^2/s^2$ |
| $\Lambda$ | = | eigenvalues matrix, |
| $\mu$ | = | dynamic viscosity, $kg/m \cdot s$ |
| $\rho$ | = | density, $kg/m^3$ |
| $\tau$ | = | shear stress, Pa |
| $\phi$ | = | shape function |
| $\psi$ | = | general function |
| $\Omega$ | = | computational domain |

*Subscripts*

| | | |
|---|---|---|
| $c$ | = | critical, centerline, cutoff |
| fd | = | fully developed |
| $h$ | = | discretized computational domain |
| $i$, $j$, $k$ | = | direction, counter |
| in | = | inlet |
| $L$ | = | lower cell index |
| $n$ | = | normal to boundary |
| out | = | outlet |
| $R$ | = | upper cell index |
| $r$, $\theta$ | = | cylindrical coordinates |
| $S$ | = | Sutherland constant, compressibility |
| $t$ | = | turbulent, tangential |
| $w$ | = | wall |
| 0 | = | reference |
| 1,2,3 | = | indices for triangle vertices |

*Superscripts*

| | | |
|---|---|---|
| $n$ | = | time-step iteration |
| $\hat{}$ | = | Roe-average quantity |

Received 17 October 2008; revision received 12 May 2009; accepted for publication 22 May 2009. 

*Professor, School of Mechanical Engineering, Azadi Avenue; anouri@sharif.edu.
†Ph.D. Student, School of Mechanical Engineering, Azadi Avenue; ziaeirad@mech.sharif.edu.
‡Professor, Institute of Turbomachinery and Fluid Dynamics, Appelstrasse 9; seume@tfd.uni-hannover.de.

$\pm$ = positive/negative eigenvalues
$+$ = $()\sqrt{k\rho\rho_w}/\mu_w$
$-$ = mean

## I. Introduction

INTERNAL compressible turbulent flow is of importance in many mechanical and aerospace applications such as heat exchangers, gas and steam turbines, reciprocating engines, gas transmission pipelines, and combustion chambers [1]. In the majority of these applications, the available duct length may be too short for establishing fully developed flow conditions and the transport phenomena are confined to what is known as an entrance region.

Although the problems concerning the internal compressible laminar boundary-layer flows have been extensively studied by numerical techniques, the validity of the turbulent flow simulation usually needs some empirical results. Wall-bounded compressible turbulent flows have been the subject of numerical studies by different groups in the past decade with the aim of finding suitable scaling to account for compressibility effects in such flows. Some of these numerical approaches have been discussed in the texts by Cebeci and Smith [2], Schreier [3], and Anderson [4]. In most practical boundary-layer calculations involving pressure gradients and heat transfer, it is necessary to predict the boundary layer over the whole length of the flow domain [5]. Most of the studies are one-dimensional and have been done in long pipes [6,7]. Ceylan and Kelbaliyev [8] investigated the effect of pipe roughness on friction factor and convective heat transfer in a fully developed turbulent flow and proposed a correlation for the friction factor in the transition region.

Browne and Dinkelacker [9] measured the mean turbulent velocity profile and longitudinal velocity fluctuation in a fully developed pipe flow by a hot-wire device in the range of $8.5 \times 10^3 < Re < 6.64 \times 10^4$. They considered the physical features of flow by fluctuations of pressure and velocity spectra and correlations between these fluctuations. De Chant [10] developed an analytical skin-friction model for an internal fully developed compressible turbulent flow under adiabatic and nonadiabatic as well as smooth and rough conditions using the incompressible law of the wall relation. His model shows an agreement with available friction-factor data within 15%.

Mohanty and Asthana [11] solved the boundary-layer equations for a supersonic perfect gas in the inlet region of a smooth circular pipe under adiabatic conditions by using the von Karman–Pohlhausen integral technique. They presented in detail the flow characteristics such as boundary-layer development, choking condition, pressure gradient, and wall shear stress for $Pr = 1$ and different inlet Mach numbers.

Xu et al. [12] presented the finite volume formulation for turbulent pipe flows with the large eddy simulation model (LES) based on three-dimensional time-dependent compressible Navier–Stokes equations in Cartesian coordinates. They employed a dual-time-stepping approach for the time derivative to simulate pipe flow efficiently at low Mach numbers. To evaluate the compressible LES finite volume formulation, they simulated turbulent pipe flow at two Reynolds numbers under isothermal and adiabatic conditions. In the case of heat transfer, temperature fluctuations and a fully developed thermal boundary layer were considered at nearly incompressible flow ($M = 0.001$).

Lin et al. [13] investigated the thermal characteristics of a laminar pipe flow subjected to a step change in ambient temperature at the entrance region by using the implicit finite difference scheme. They reported the axial variation of the modified Nusselt number, wall and bulk fluid temperatures, and the transient temperature profiles at certain axial locations for various outside heat transfer coefficients.

In this study, to transfer a compressible flow through a pipeline with high efficiency, a thorough description of physical phenomena has been numerically investigated in compressible turbulent flow. The development of the physical phenomena includes both the developing and the developed regions. Also, the effects of heat transfer and skin friction on the compressible turbulent flow has been considered.

## II. Mathematical Formulation

Figure 1 shows a two-dimensional compressible pipe flow with boundary-layer development in the entrance region under a constant wall heat flux. The unsteady versions of mass, momentum in the $z$ and $r$ directions, energy equations in a conservation form for a two-dimensional compressible flow in cylindrical coordinates, and the equation of state for a perfect gas are, respectively,

$$\frac{\partial \rho}{\partial t} + \frac{\partial(\rho u_z)}{\partial z} + \frac{1}{r}\frac{\partial(r\rho u_r)}{\partial r} = 0 \tag{1}$$

$$\frac{\partial(\rho u_z)}{\partial t} + \frac{\partial(\rho u_z^2 + p)}{\partial z} + \frac{1}{r}\frac{\partial(r\rho u_r u_z)}{\partial r} = \frac{\partial \tau_{zz}}{\partial z} + \frac{1}{r}\frac{\partial(r\tau_{rz})}{\partial r} \tag{2}$$

$$\frac{\partial(\rho u_r)}{\partial t} + \frac{\partial(\rho u_r u_z)}{\partial z} + \frac{1}{r}\frac{\partial[r(\rho u_r^2 + p)]}{\partial r} = \frac{\partial \tau_{zr}}{\partial z} + \frac{1}{r}\frac{\partial(r\tau_{rr})}{\partial r} - \frac{\tau_{\theta\theta}}{r} \tag{3}$$

$$\frac{\partial(\rho e_t)}{\partial t} + \frac{\partial[(\rho e_t + p)u_z]}{\partial z} + \frac{1}{r}\frac{\partial[r(\rho e_t + p)u_r]}{\partial r} = \frac{\partial b_z}{\partial z} + \frac{1}{r}\frac{\partial(rb_r)}{\partial r} \tag{4}$$

$$p = \rho(\gamma - 1)[e_t - \tfrac{1}{2}(u_z^2 + u_r^2)] \tag{5}$$

where $u_z$ and $u_r$ are the axial and radial velocity components, respectively, and $e_t$ is the total internal energy. The sum of heat flux and surface work done by frictional forces in the energy equation is

$$b_j = \gamma\left(\frac{\mu}{Pr} + \frac{\mu_t}{Pr_t}\right)\frac{\partial T}{\partial j} + u_j\tau_{jj} + u_i\tau_{ji} \tag{6}$$

where $j = z$ or $r$ and $i = r$ or $z$. $Pr_t = 0.9$ is the turbulent Prandtl number.

The turbulent shear stresses are

$$\tau_{zz} = (\mu + \mu_t)\left[2\frac{\partial u_z}{\partial z} - \frac{2}{3}(\nabla \cdot \mathbf{V})\right] \tag{7}$$

$$\tau_{zr} = (\mu + \mu_t)\left[\frac{\partial u_z}{\partial r} + \frac{\partial u_r}{\partial z}\right] \tag{8}$$

$$\tau_{rr} = (\mu + \mu_t)\left[2\frac{\partial u_r}{\partial z} - \frac{2}{3}(\nabla \cdot \mathbf{V})\right] \tag{9}$$

$$\tau_{\theta\theta} = (\mu + \mu_t)\left[2\frac{u_r}{r} - \frac{2}{3}(\nabla \cdot \mathbf{V})\right] \tag{10}$$

where $\nabla \cdot \mathbf{V} = \partial u_z/\partial z + \partial(ru_r)/r\partial r$.

### A. Core-Region Turbulence Modeling

The turbulent viscosity in the regions somewhat far from the walls is modeled:

$$\mu_t = c_\mu \rho \frac{\kappa^2}{\varepsilon} \tag{11}$$

where $c_\mu = 0.09$. The equations of turbulent kinetic energy and its dissipation rate including the compressibility effect for high Mach number flows are, respectively,

$$\frac{\partial(\rho\kappa)}{\partial t} + \nabla \cdot (\rho\kappa V) = \frac{\partial}{\partial z}\left[(\mu + \mu_t)\frac{\partial \kappa}{\partial z}\right] + \frac{1}{r}\frac{\partial}{\partial r}\left[r(\mu + \mu_t)\frac{\partial \kappa}{\partial r}\right] + \mu_t P - \frac{2}{3}\rho\kappa D - \rho\varepsilon_S \tag{12}$$

$$\frac{\partial(\rho\varepsilon)}{\partial t}+\nabla\cdot(\rho\varepsilon V)=\frac{\partial}{\partial z}\left[(\mu+C_\varepsilon\mu_t)\frac{\partial\varepsilon}{\partial z}\right]+\frac{1}{r}\frac{\partial}{\partial r}\left[r(\mu+C_\varepsilon\mu_t)\frac{\partial\varepsilon}{\partial r}\right]+c_1\rho\kappa P-\frac{2c_1}{3c_\mu}\rho\varepsilon_S D-c_2\rho\frac{\varepsilon_S^2}{\kappa} \quad (13)$$

where $c_\varepsilon=0.07$, $c_1=0.129$, and $c_2=1.83$.

Wilcox [14] proposed the compressibility dissipation in terms of the incompressibility dissipation as

$$\frac{\varepsilon_s}{\varepsilon}=1+\left\{1-\exp\left[-\frac{(M_t-M_c)^2}{\Lambda^2}\right]\right\}H(M_t-M_c) \quad (14)$$

where $\Lambda=0.66$, and $H(M_t\geq M_c)=1$ or $H(M_t<M_c)=0$ is the Heaviside step function.

The compressibility modification takes effect when the turbulent Mach number, $M_t^2=2\kappa/c^2$, is more than the cutoff turbulent Mach number, $M_c=0.25$, where subscript $c$ indicates speed of sound.

In Eqs. (12) and (13), the destruction and production terms are, respectively,

$$D=\frac{\partial u_z}{\partial z}+\frac{\partial u_r}{\partial r}$$
$$P=\left(\frac{\partial u_z}{\partial r}+\frac{\partial u_r}{\partial z}\right)^2+\frac{4}{3}\left[\left(\frac{\partial u_z}{\partial z}\right)^2+\left(\frac{\partial u_r}{\partial r}\right)^2-\frac{\partial u_z}{\partial z}\frac{\partial u_r}{\partial r}\right] \quad (15)$$

Because this choice leads to an overprediction of the eddy viscosity, therefore, we drop the dissipation term and only keep the shear based component in $P$ as

$$P=\left(\frac{\partial u_z}{\partial r}+\frac{\partial u_r}{\partial z}\right)^2 \quad (16)$$

The temperature-dependent molecular viscosity is based on the Sutherland law:

$$\mu=\mu_0\frac{T_0+T_S}{T+T_S}\left(\frac{T}{T_0}\right)^{1.5} \quad (17)$$

where $T_S$ is the Sutherland constant temperature, which is 110 K for air.

### B. Near-Wall Turbulence Modeling

The classical $\kappa$-$\varepsilon$ model validated under the hypothesis of a high local Reynolds number is not adequate for describing regions close to the wall. In this case, two approaches can model the near-wall region. In the wall function approach used in most high Reynolds number flows, the viscosity-affected inner region (viscous sublayer and buffer layer) is not resolved. Instead, it is bridged by a semi-empirical formula between the wall and the fully turbulent region. In another approach used in a low Reynolds number flow, the viscosity-affected inner region is solved with a mesh all the way down to the wall. Such situations require near-wall models that are valid in the viscosity-affected region. The latter approach is modeled and used in this work; to compute the viscosity-affected near-wall region, the equation of Wolfstein [15] is employed:

$$\frac{\partial(\rho\kappa)}{\partial t}+\nabla\cdot(\rho u\kappa)-\nabla\cdot[(\mu+\mu_t)\nabla\kappa]=\mu_t\cdot P-\rho\frac{\kappa^{3/2}}{l_\varepsilon} \quad (18)$$

where

$$l_\varepsilon=c_4c_\mu^{-0.75}[1-\exp(-y^+/2c_4c_\mu^{-0.75})]y$$

However, the turbulent viscosity is computed from

$$\mu_t=c_\mu\rho l_\mu\sqrt{\kappa} \quad (19)$$

where $l_\mu=0.41c_\mu^{-0.75}[1-\exp(-y^+/70)]y$

The method enables us to compute the flow from the wall up to $y^+=y\sqrt{k\rho\rho_w}/\mu_w<200$ with more computational resources as a result of a finer mesh size.

Looking at the conservative form of the governing equations, we note that they all have the same generic form:

$$\frac{\partial Q}{\partial t}+\nabla\cdot F(Q)=\nabla\cdot N(Q)+S(Q) \quad (20)$$

where $Q$, $F(Q)$, $N(Q)$, and $S(Q)$ are the conservative variables, inviscid flux, viscous flux, and source vector, respectively, and

$$Q=[\ \rho\quad \rho u_z\quad \rho u_r\quad \rho e_t\quad \rho\kappa\quad \rho\varepsilon\ ]^T \quad (21)$$

The inviscid flux vector $F(Q)$ includes components $F_z(Q)$ and $F_r(Q)$ with the following expressions:

$$F_j(Q)=[\ \rho u_j\quad \rho u_iu_j\quad \rho u_j^2+p\quad (\rho e_t+p)u_j\quad \rho u_j\kappa\quad \rho u_j\varepsilon\ ]^T$$
$$i\ \text{ or }\ j=z\ \text{ or }\ r \quad (22)$$

The viscous flux vector $N(Q)$ also includes $N_z(Q)$ and $N_r(Q)$ with the following forms:

$$N_j(Q)=\left[\ 0\quad \tau_{ij}\quad \tau_{jj}\quad b_j\quad (\mu+\mu_t)\tfrac{\partial\kappa}{\partial j}\quad (\mu+C_\varepsilon\mu_t)\tfrac{\partial\varepsilon}{\partial j}\ \right]^T$$
$$i\ \text{ or }\ j=z\ \text{ or }\ r \quad (23)$$

The source vector for axisymmetric flow is written as

$$S(Q)=[\ 0\quad 0\quad -\tau_{\theta\theta}/r\quad 0\quad S_\kappa\quad S_\varepsilon\ ]^T \quad (24)$$

## III. Numerical Technique

The preceding governing equations of the compressible viscous turbulent flow are solved by the finite volume Galerkin upwind technique using the Roe [16] Riemann solver for the convective terms and standard Galerkin technique for the viscous terms. The discretization will be carried out on a generally unstructured triangular mesh.

### A. Computational Domain and Integral Approximation

Figure 2 shows grid nodes and discretization of computational domain $\Omega=K_jC_j=K_iA_i$ by triangles (for the viscous part) and hexagonal cells (for the inviscid part), where $C_j(A_i)$ is a triangle (hexagonal) cell and $K_j(K_i)$ is the number of total triangles (hexagonals). The variables computed on nodes are denoted by subscript $h$. If the nodes are the vertices of triangle elements, they form a finite element grid; otherwise, they form a control volume in the center of a hexagonal finite volume grid.

The weak finite element formulation of the general equation (20) without the source term can be written as

$$\int_\Omega\frac{\partial Q_h}{\partial t}\phi_h\,dA+\int_\Omega\nabla\cdot(F_h-N_h)\phi_h\,dA=0 \quad (25)$$

where $\phi$ is the shape function. In the finite volume calculations, it is equal to 1. In the finite elements, it is computed from the geometry and is used for computing the derivatives that appear in the viscous terms on each triangle. Changing the integral of the viscous term $N$ using integration by parts and leaving the convective term $F$ unchanged with a shape function equal to 1, the result is

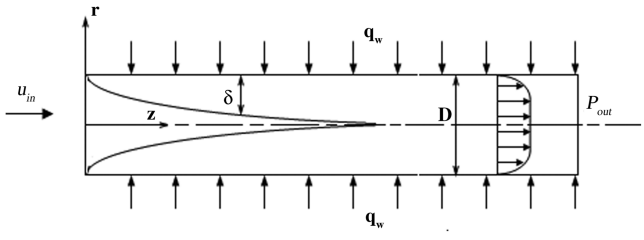


**Fig. 1 Schematic of two-dimensional pipe flow with boundary-layer development.**

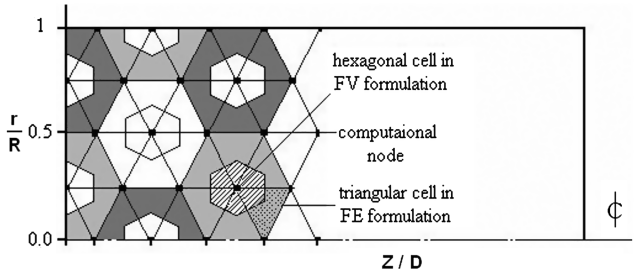


**Fig. 2 A schematic of grid arrangement and computational domain Ω in half of the pipe (FV denotes finite volume and FE denotes finite element).**

### C. Discretization of Inviscid Parts

In each triangle, we suppose that the vector $F$ [Eq. (22)] varies linearly from one side to the other. The convection term on the left-hand side is evaluated by the finite volume Roe method [16] on the control volume surfaces, which are the sides of the hexagonal shape. The flux vector across these planes will be

$$F = \tfrac{1}{2}(F_L + F_R) - \tfrac{1}{2}R|\Lambda|R^{-1}\Delta Q \tag{31}$$

where $F_L$ and $F_R$ are computed from $Q_L$ and $Q_R$, respectively. $\Delta Q = Q_R - Q_L$. $|\Lambda|$, and $R$ are the matrices of eigenvalues and eigenvectors of the flux Jacobian matrix $A$ as

$$A = \frac{\partial F}{\partial Q} = \begin{bmatrix} 0 & n_z & n_r & 0 \\ -u_z u_n + \frac{\gamma-1}{2}(u_z^2 + u_r^2)n_z & (2-\gamma)u_z n_z + u_n & -\gamma u_r n_z + u_t & (\gamma-1)n_z \\ -u_r u_n + \frac{\gamma-1}{2}(u_z^2 + u_r^2)n_r & -\gamma u_z n_r + u_t & (2-\gamma)u_r n_r + u_n & (\gamma-1)n_r \\ \left[-H + \frac{\gamma-1}{2}(u_z^2 + u_r^2)\right]u_n & -Hu_z + (1-\gamma)u_n & -Hu_r + (1-\gamma)u_n & \gamma u_n \end{bmatrix} \tag{32}$$

$$\int_\Omega \frac{\partial Q_h}{\partial t}\phi_h \,\mathrm{d}A + \int_\Omega \nabla \cdot F_h \,\mathrm{d}A + \int_\Omega N_h \nabla \phi_h \,\mathrm{d}A - \int_{\partial\Omega} N_h \cdot n\phi_h \,\mathrm{d}C = 0 \tag{26}$$

where $\partial\Omega$ signifies the boundary of the triangles in the domain. Using the explicit time integration and introducing the divergence theorem for the convective part, the results are

$$|A_i|\frac{Q^{n+1} - Q^n}{\Delta t} + \int_{\partial C_i} F_d \cdot n \,\mathrm{d}C = -\int_{\Omega_h} N_h \nabla \phi_h \,\mathrm{d}A + \int_{\partial\Omega} N_h \cdot n\phi_h \,\mathrm{d}C \tag{27}$$

where the superscripts $n$ and $n+1$ denote old and new time steps, respectively. The index $d$ shows that the integral should be computed on the hexagonal edges. The domain $\partial C_i$ denotes the boundary of hexagonal grids. The second term on the right-hand side is related to the boundary condition, which is set to zero herein. The boundary condition will be applied in the finite volume formulation of convective terms.

### B. Discretization of Viscous Parts

A central scheme is used to compute the viscous term on each cell. For a triangle with vertices 1, 2, and 3, the gradients of the shape functions in the $z$ and $r$ directions are defined as

$$\frac{\partial \phi_i}{\partial z} = r_j - r_k, \qquad \frac{\partial \phi_i}{\partial r} = z_k - z_j, \qquad i, j, k = 1, 2, 3 \tag{28}$$

The derivative of each primitive variable (i.e., $\rho$, $u_z$, $u_r$, and $p$) can be computed by the following relation:

$$\frac{\partial \psi}{\partial n} = \psi_1 \frac{\partial \phi_1}{\partial n} + \psi_2 \frac{\partial \phi_2}{\partial n} + \psi_3 \frac{\partial \phi_3}{\partial n}, \qquad n = z \quad \text{or} \quad r \tag{29}$$

The mean values of the velocity components and viscosity on each triangle used in the computation of deformation tensor components, and viscous dissipation terms can be obtained as

$$\bar{u}_{r,z} = \tfrac{1}{3}(u_{r,z,1} + u_{r,z,2} + u_{r,z,3}), \qquad \bar{\mu} = \tfrac{1}{3}(\mu_1 + \mu_2 + \mu_3) \tag{30}$$

The eigenvalues and eigenvector matrix of $A$ are given, respectively, by

$$\lambda_1 = \lambda_2 = \hat{u}_n, \qquad \lambda_3 = \hat{u}_n + \hat{c}, \qquad \lambda_4 = \hat{u}_n - \hat{c} \tag{33}$$

$$R = \begin{bmatrix} 1 & 0 & 1 & 1 \\ \hat{u}_z - \hat{c}\cdot n_z & -\hat{u}_t n_r & \hat{u}_z & \hat{u}_z + \hat{c}\cdot n_z \\ \hat{u}_r - \hat{c}\cdot n_r & \hat{u}_t n_z & \hat{u}_r & \hat{u}_r + \hat{c}\cdot n_r \\ \hat{H} - \hat{u}_n\hat{c} & \hat{u}_t^2 & \frac{1}{2}(\hat{u}_z^2 + \hat{u}_r^2) & \hat{H} + \hat{u}_n\hat{c} \end{bmatrix} \tag{34}$$

where $\hat{c}$ is the speed of sound. The hatted normal and tangential velocity components as well as the hatted axial and radial velocity components are defined as

$$\hat{u}_n = \hat{u}_z n_z + \hat{u}_r n_r, \qquad \hat{u}_t = \hat{u}_r n_z - \hat{u}_z n_r \tag{35}$$

$$\hat{u}_z = \frac{u_{z,L}\sqrt{\rho_L} + u_{z,R}\sqrt{\rho_R}}{\sqrt{\rho_L} + \sqrt{\rho_R}}, \qquad \hat{u}_r = \frac{u_{r,L}\sqrt{\rho_L} + u_{r,R}\sqrt{\rho_R}}{\sqrt{\rho_L} + \sqrt{\rho_R}}$$
$$\hat{H}_z = \frac{H_L\sqrt{\rho_L} + H_R\sqrt{\rho_R}}{\sqrt{\rho_L} + \sqrt{\rho_R}} \tag{36}$$

The other quantities with hats in eigenvector arrays are not averaged independently, but are the basic Roe-averaged quantities by their normal functional relation [16].

### D. Axisymmetric Corrections

The difference between the terms in cylindrical and Cartesian coordinate systems in the weak form of the Navier–Stokes equations comes from the differential area in the integrals ($r\,\mathrm{d}r\,\mathrm{d}z$ replaced by $\mathrm{d}r\,\mathrm{d}z$). So we multiply the cell areas $|A_i|(|C_i|)$ and the length of the computational domain edges by some radius $r$ obtained from the radius of the nodes $r_i$. The other modification comes from the additional source terms occurring in the governing equation. Now, by transferring the additional terms of the cylindrical coordinates, compared with the Cartesian coordinates, to the right-hand side of the governing equation, the left-hand side of the equation can be solved by the Cartesian coordinate algorithm. For instance, the following integrals are added in the $z$ and $r$ directions of the momentum equation and the energy equation, respectively:

$$-\int_{\partial C_i} \frac{2}{3}(\mu + \mu_t)u_r n_z \,\mathrm{d}C \tag{37}$$

$$-\int_{C_i}\frac{P}{r}r\,\mathrm{d}r\,\mathrm{d}z-\int_{C_i}\frac{\tau_{\theta\theta}}{r}r\,\mathrm{d}r\,\mathrm{d}z-\int_{\partial C_i}\frac{2}{3}(\mu+\mu_t)u_r n_r\,\mathrm{d}C \quad (38)$$

$$-\int_{\partial C_i}\frac{2}{3}(\mu+\mu_t)u_z u_r n_z\,\mathrm{d}C-\int_{\partial C_i}\frac{2}{3}(\mu+\mu_t)u_r^2 n_r\,\mathrm{d}C \quad (39)$$

### E. Integration Procedure

If Eq. (20) is rewritten explicitly in time as follows, the right-hand side of the equation will contain all convective, viscous, and source terms. Then an iterative scheme is used to reach a steady solution:

$$\frac{\partial Q}{\partial t}=\mathrm{RHS}(Q) \quad (40)$$

where $\mathrm{RHS}(Q)$ is the right-hand side term.

The time integration procedure has been carried out using a fourth-order Runge–Kutta scheme as

$$Q_0=Q^n$$
$$Q_i=Q_i+\alpha_i\frac{\Delta t}{|A|}\mathrm{RHS}(Q_{i-1}),\quad i=1,2,3,4$$
$$Q^{n+1}=Q_4 \quad (41)$$

where $\mathrm{RHS}(Q_{i-1})$ is evaluated at the previous time step. The scheme enables us to investigate the treatment of steady-state flow when the desired degree of convergence is achieved.

### F. Boundary and Initial Conditions

On the tube wall with no-slip condition $\mathbf{V}=0$ and on the pipe axis, the symmetry boundary condition is $\mathbf{V}\cdot\mathbf{n}=0$. If the wall is subjected to a constant heat flux, the fourth term of Eq. (27) should be evaluated and corrected explicitly in each iteration as

$$\int_{\partial\Omega}N_h\cdot n\phi_h\,\mathrm{d}C=\int_{\partial\Omega}q_h''\,\mathrm{d}C \quad (42)$$

In subsonic flow, the inflow boundary condition requires three specified primitive variables, whereas at the outflow, only one primitive variable should be specified. They are treated by a new method of characteristics technique such that the fluxes are split into positive and negative parts following the sign of the eigenvalues of the Jacobian matrix $A=\partial F/\partial Q$ [17]:

$$\int_{C_\infty}F\cdot n\,\mathrm{d}C=\int_{C_\infty}(A^+Q_{\mathrm{in}}+A^-Q_{\mathrm{out}})\cdot n\,\mathrm{d}C \quad (43)$$

where $A^+$ and $A^-$ are positive and negative parts of Jacobian matrix, respectively, and are defined by

$$A^+=R|\Lambda^+|R^{-1},\qquad A^-=R|\Lambda^-|R^{-1} \quad (44)$$

At the inlet, $Q_{\mathrm{in}}$ is the interior value and determined by the interior values of the previous iteration. $Q_{\mathrm{out}}$ is the exterior value and given by the flow configuration. In the steady-state subsonic flow, the $Q_{\mathrm{out}}$ values depend on employing density, static pressure, and the radial velocity component, which is usually zero for simplicity. The axial velocity component $u_z$ belongs to $Q_{\mathrm{in}}$ and is determined by the characteristic property and convected outward with respect to the computational domain, similar to the interior values of $Q_{\mathrm{in}}$. At the outlet, $Q_{\mathrm{out}}$ depends only on the static pressure and the other three conditions are the characteristic variables convected toward the exterior of the domain. It is set equal to the interior of the previous iteration similar to $Q_{\mathrm{in}}$ again. Under the adiabatic condition, the steady-state solution is used as an initial condition and the inflow turbulent kinetic energy and its dissipation are set equal to zero.

## IV. Numerical Accuracy

The numerical solution accuracy of the assumed mathematical model has been verified by comparison between the results of the present work with experimental and numerical data of the previous workers. These comparisons are discussed in the next section.

To show sensitivity of important dependent variables on spatial grids, the spatial discretization error was checked by the global conservation of mass balance between the inflow and outflow in the steady-state condition. The result showed that the variation of the mass flow rate along the pipe was not more that 1%. Also, to illustrate sensitivity of the dependent variables on time step, the temporal discretization error was quantified by the classical Courant–Friedrichs–Lewy (CFL) stability criterion used explicitly in the numerical calculations. The value of $\mathrm{CFL}=1$ was used in the computation with $\kappa$-$\varepsilon$ turbulence modeling. The minimum time step between that defined according to CFL number definition for inviscid flow and that for viscous flow was

$$\Delta t_i=\mathrm{CFL}\times\min\left[\frac{|u|+c}{\Delta x}+\frac{2\gamma}{Pr}\times\frac{\mu+\mu_t}{\rho\Delta x^2}\right]^{-1} \quad (45)$$

where $\Delta x$ was the minimum height of the triangles having node $i$ in common. As this result was obtained from one-dimensional stability analysis, in fact, it was too restrictive. Thus, we could take only the first term in the bracket, but this is not always true.

To indicate the accuracy of convergence of the iterative scheme in the numerical solution, the convergence history of conservative variables toward a steady-state solution is depicted in Fig. 3. The figure is prepared for an adiabatic compressible flow with $Re_{\mathrm{in}}=1.6\times10^6$, $M_{\mathrm{in}}=0.34$, and $L/D=50$. The variables consist of density, momentum in the $z$ and $r$ directions, and energy per unit volume. The computational domain includes $101\times151$ grids in the radial and axial directions, respectively. The convergence criterion of the iterative scheme was based on the absolute residual value for each variable and was less than $10^{-8}$. The residual value was obtained by summation of each grid residual over the entire domain and normalized by its first iteration value. The results showed that the mass and energy balances were satisfied after about 1000 iterations, whereas the axial momentum balanced after $4\times10^4$ iterations.

## V. Results and Discussion

Because of the axial symmetry, half of the pipe is used as a computational domain (Fig. 2). An unstructured triangular grid in the $z$ and $r$ directions is employed. To get a sufficient resolution, the mesh size is refined in the boundary-layer region according to a $y^+$ limitation for turbulence models, which is measured from the pipe wall toward the inside. Additionally, several mesh sizes were tested to ensure that the results of the numerical solution are mesh-size-independent. The area size of the computational domain is $R\times100R$ and consists of 101 uniform meshes in the $z$ and 151 nonuniform

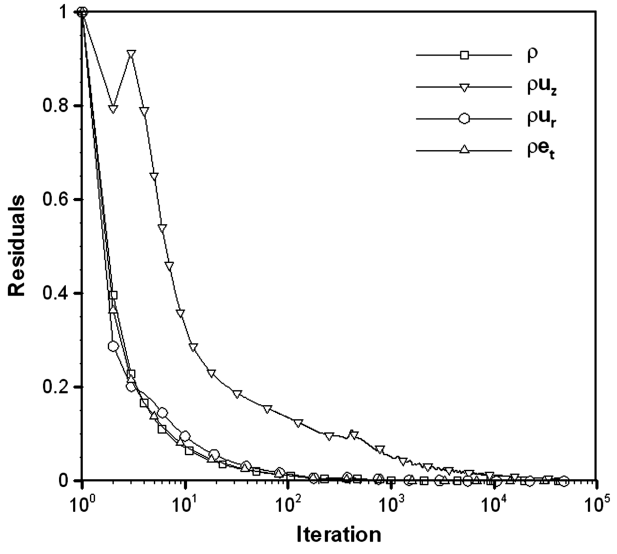


**Fig. 3 Convergence history of the conservative variables.**

meshes in the $r$ direction. The nodes are packed near the wall such that there are three nodes within the distance of $y^+ < 10$. The first node is located at $y^+ = 1$ according to the criteria of the two-layer turbulent model. The location of the grid nodes with nonuniform spacing in the $r$ direction is obtained by the following relation:

$$\frac{r}{R} = 1 + (\beta + 1)\frac{[(\beta + 1)/(\beta - 1)]^{\xi - 1} - 1}{[(\beta + 1)/(\beta - 1)]^{\xi} + 1} \tag{46}$$

where $\beta = 1.3$, $0 \le \xi = j\Delta r/R < 1$, and $j = 1, 2, 3, \ldots, N_r = R/\Delta r$.

### A. Isothermal Flow with High Inlet Mach Numbers

To validate the numerical solution, a turbulent airflow was considered in the entrance region of a pipe with a uniform wall temperature of 330 K. The inlet freestream properties were used as the initial conditions at each grid point with $4 \times 10^4$ number of iterations. The inflow air had a total pressure of 1 bar, a total temperature of 288.5 K, and a Mach number of 0.34. These conditions at the inflow gave a bulk Reynolds number $Re = 1.6 \times 10^6$ and the inlet-to-outlet pressure ratio was $p_{\text{out}}/p_{\text{in}} = 0.945$. The reference temperature, velocity, and pressure were $T_0 = 282$ K, $u_0 = 114.4$ m/s, and $p_0 = 0.93$ bar, respectively. Also, the pipe wall roughness and the air Prandtl number were set to $\varepsilon = 4.6 \times 10^{-5}$ m and $Pr = 0.71$.

Figures 4 and 5 show the centerline velocity and pressure along the pipe, respectively, compared with the numerical results of Wang et al. [18] and experimental data of Ward-Smith [19]. The flow velocity profile does not reach a fully developed condition at $Z/D = 50$, because in compressible flow, the velocity profile increases continuously along the pipe. However, there is a good agreement between the centerline velocity of the present work and the experimental data [19] in the range of $0 < Z/D < 50$. This agreement no longer holds after $Z/D = 10$ between the present work and the numerical results of Wang et al. [18] using a Baldwin–Lomax eddy viscosity model.

Figures 6 and 7 illustrate the distribution of friction factor and Nusselt number along the pipe. In these figures, the mesh size is uniform in the $z$ direction, but clustered toward the wall, with the smallest mesh size of $y^+ = 1$ and a stretching ratio of $\beta = 1.01$. The numerical results of Wang et al. [18] computed with uniform grid node spacing show that the friction factor increases a little after $Z/D > 30$, but the Nusselt number always decreases. The same behavior is seen in the present work if more grid nodes are used in the $z$ direction (more than 301 points). For comparison, the friction factor and Nusselt number of a fully developed incompressible turbulent

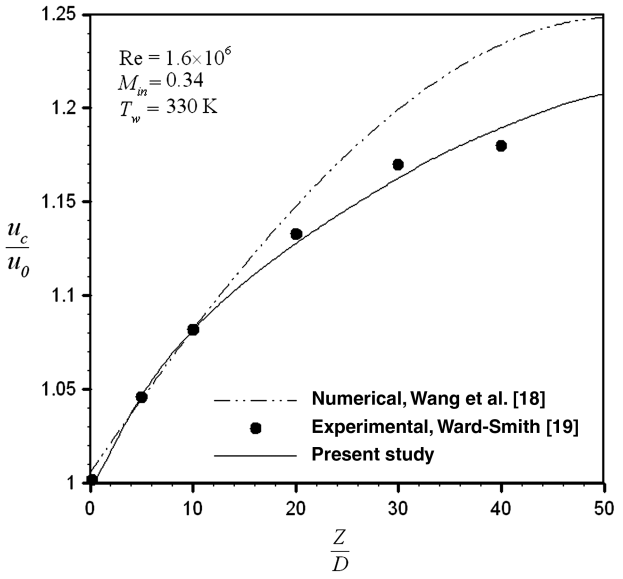


Fig. 4 Centerline velocity along the pipe.

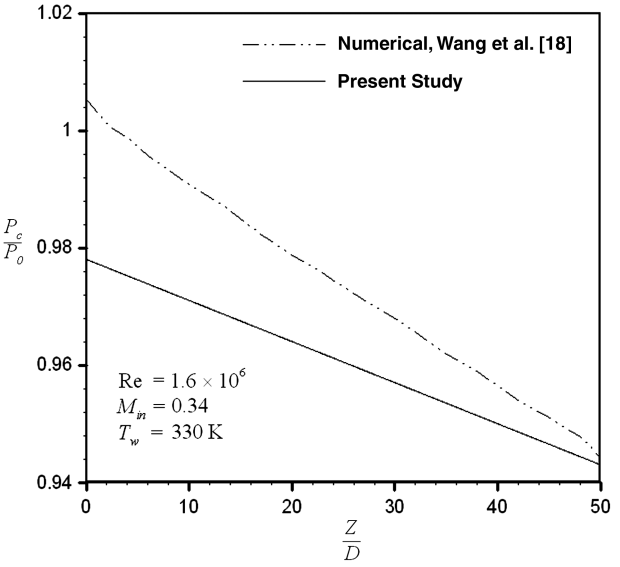


Fig. 5 Centerline static pressure along the pipe.

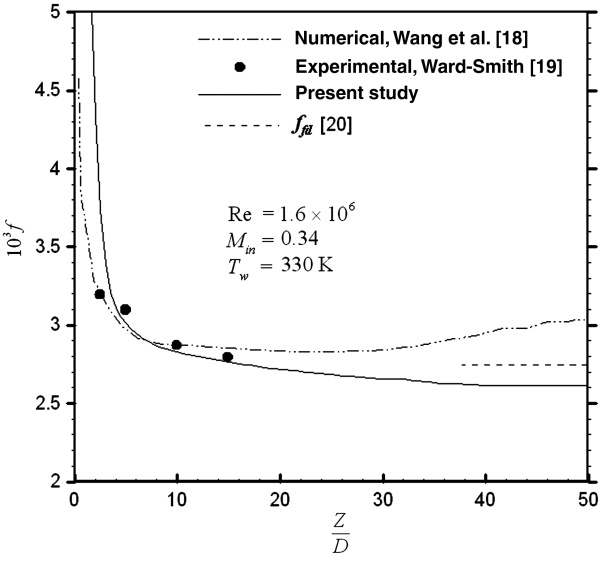


Fig. 6 Skin-friction factor along the pipe.

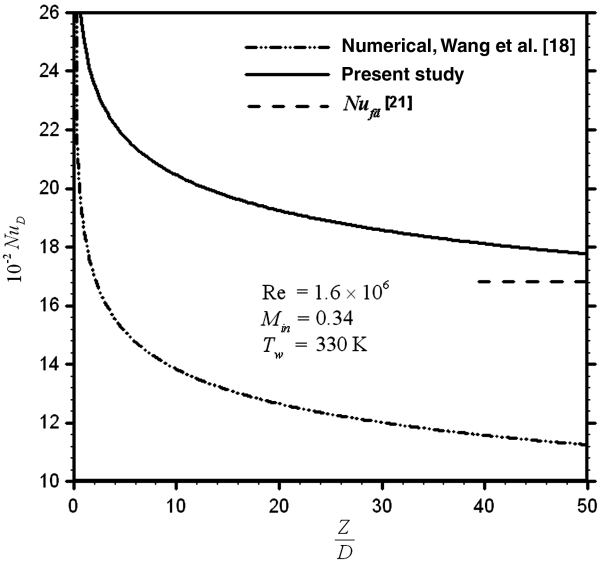


Fig. 7 Nusselt number along the pipe.

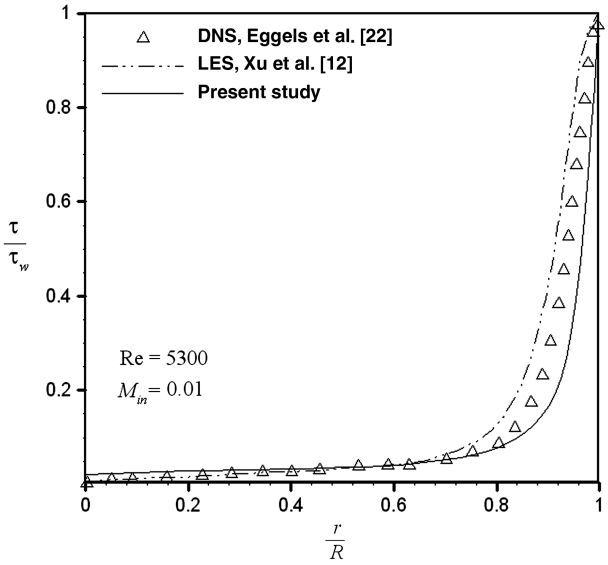


**Fig. 8 Fully developed shear stress across the pipe.**

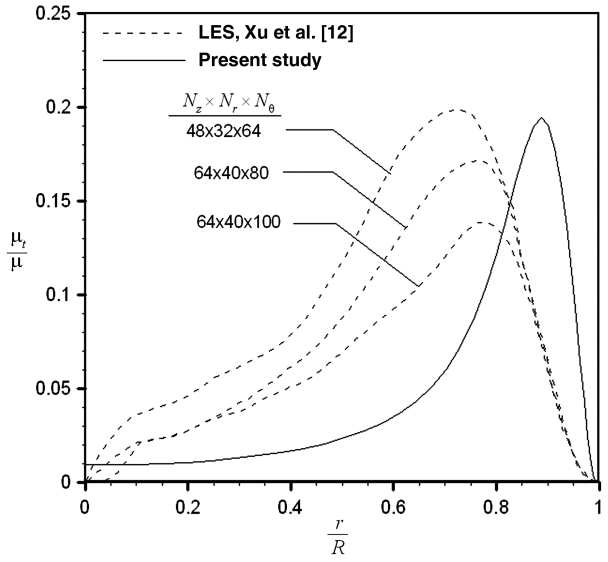


**Fig. 9 Turbulent viscosity across the pipe.**

pipe flow are indicated in the two figures and their values are $f_{\text{fd}} = 2.74 \times 10^{-3}$ and $Nu_{\text{fd}} = 1685$. These values are calculated by Haaland's correlation [20] and Gnielinski's correlation [21].

### B. Isothermal Flow with Low Mach Numbers

Figure 8 shows the distribution of the shear stress across the pipe for the inlet Mach number $M_{\text{in}} = 0.01$ and Reynolds number of $Re = 5300$. The ordinate of the figure has been nondimensionalized by the wall shear stress. To assure mesh size independence, the numerical calculations had been done for two grids resolutions of $128 \times 80$ and $128 \times 40$ in the $z$ and $r$ directions, respectively. The difference between their results is insignificant. The mesh size is

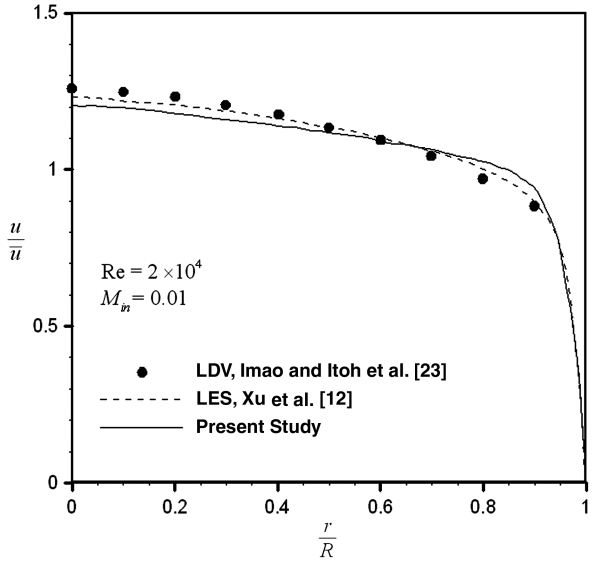


**Fig. 10 Fully developed axial velocity across the pipe.**

uniform in the $z$ direction, but refined toward to the wall, with the smallest mesh size of $y^+ = 1$ and a stretching ratio of $\beta = 1.05$. To validate the present results, the numerical results of Xu et al. [12] and Eggels et al. [22] are added in the figure based on two turbulent models of direct numerical simulation (DNS) and LES with grid resolution of $256 \times 96 \times 128$ in the axial, radial, and circumferential directions, respectively. This figure exhibits that the flow shear stress is nearly constant from the centerline up to 75% of the pipe radius, then increases sharply next to the wall, whereas this behavior is linear for the incompressible flow across the pipe from the centerline to the wall.

Figure 9 illustrates the fully developed turbulent viscosity relative to the molecular viscosity across the pipe at different axial positions. The results of subgrid-scale modeling by Xu et al. [12] are added. Although the value of the turbulent viscosity in the fully developed region is very close to that modeled by the LES method, it does not exactly match the present results. As the figure indicates, the ratio of the turbulent viscosity to the molecular one is less than 0.2, whereas it is greater than 1 for the incompressible flow and this in itself is a significant difference between internal compressible and incompressible flow.

Figure 10 depicts the fully developed axial velocity relative to the bulk velocity across the pipe for $Re = 2 \times 10^4$ and $M_{\text{in}} = 0.01$. For this case, the grid resolution is $81 \times 81$ in the $z$ and $r$ directions, respectively. The figure also shows the numerical results of Xu et al. [12] obtained by the LES turbulence model and the experimental data of Imao and Itoh [23]. These data are obtained by using a single-component laser-Doppler velocimeter. As we can see, there is a good agreement between the present results with the available results.

### C. Flow with Uniform Wall Heat Flux

Table 1 lists the skin-friction factor of a fully developed adiabatic compressible flow for different grid resolutions. The grid sizes are uniform in the $z$ direction and refined with a maximum stretching ratio of $\beta = 1.05$ in the $r$ direction. The Reynolds number is $Re = 1.6 \times 10^6$, inlet Mach number $M_{\text{in}} = 0.34$, and $D = 0.7$ m. The results show that the friction factor does not change significantly after $300 \times 150$ grid nodes.

**Table 1 Grid-spacing size dependence on fully developed skin-friction factor of the pipe flow**

| $N_z \times N_r$ | $128 \times 40$ | $128 \times 50$ | $200 \times 50$ | $200 \times 100$ | $300 \times 100$ | $300 \times 150$ | $400 \times 150$ | $500 \times 150$ |
|---|---|---|---|---|---|---|---|---|
| $\Delta z/\Delta r$ | 31.25 | 39.06 | 25 | 50 | 33.33 | 50 | 37.5 | 30 |
| $f_{\text{fd}}$ | 2.22 | 2.53 | 1.91 | 2.55 | 2.50 | 2.61 | 2.63 | 2.63 |

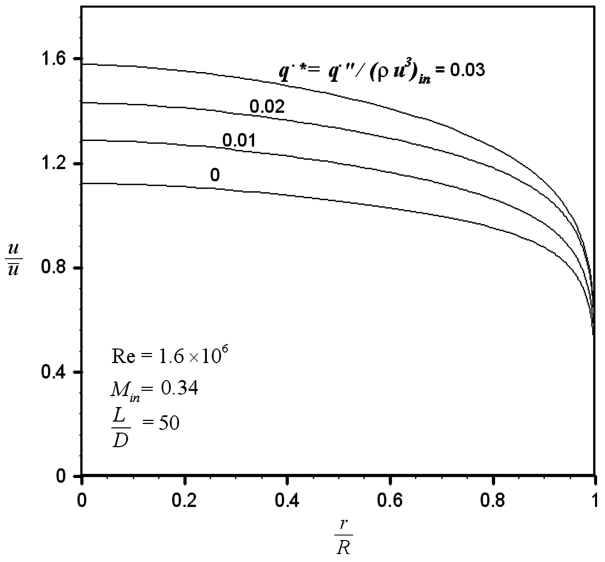


**Fig. 11 Fully developed axial velocity across the pipe for different heat fluxes.**

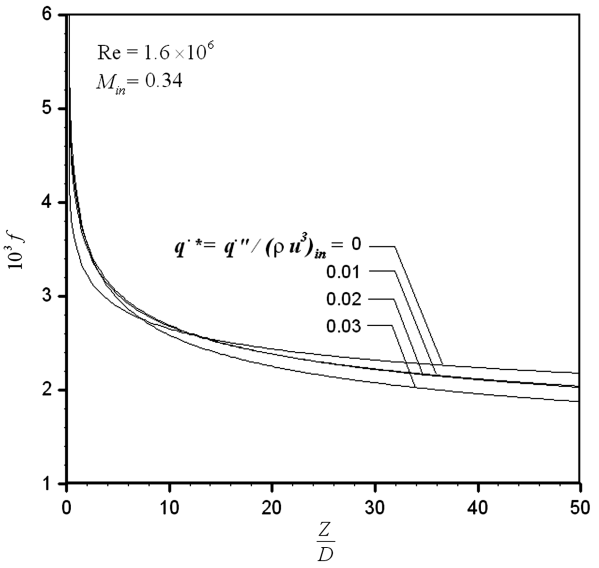


**Fig. 13 Skin-friction factor along the pipe for different wall heat fluxes.**

Figures 11 and 12 depict the effect of wall heating on the fully developed axial and centerline velocity profiles across and along the pipe, respectively, at different wall heat fluxes. With increasing heat flux, the velocity accelerates in such a way that the fully developed axial velocity becomes more similar to a parabolic shape and the entrance length of the centerline velocity increases. The dimensionless heat flux is defined by $\dot{q}^* = \dot{q}''/(\rho u^3)_{\text{in}}$.

Figures 13 and 14 exhibit the distribution of the friction factor and Nusselt number along the pipe for different values of the dimensionless wall heat flux. For instance, for $Re = 1.6 \times 10^6$, $M_{\text{in}} = 0.34$, and $D = 0.7$ m, the heat flux of $\dot{q}^* = 0.03$ is corresponding to $\dot{q}^* = 1489$ W/m$^2$. It is clear that the friction factor decreases with increasing the wall heat flux and becomes fully developed at $Z/D > 50$, whereas the Nusselt number increases with increasing heat flux and becomes fully developed at about $Z/D > 10$.

The development of the hydrodynamic boundary layer along the pipe for different wall heat fluxes is reported in Fig. 15. This figure shows that the boundary-layer thickness will increase more rapidly with more heating. This means that the fully developed velocity profile occurs sooner in the case of more wall heating. Figure 16 depicts the centerline pressure distribution along the pipe. Imposing a

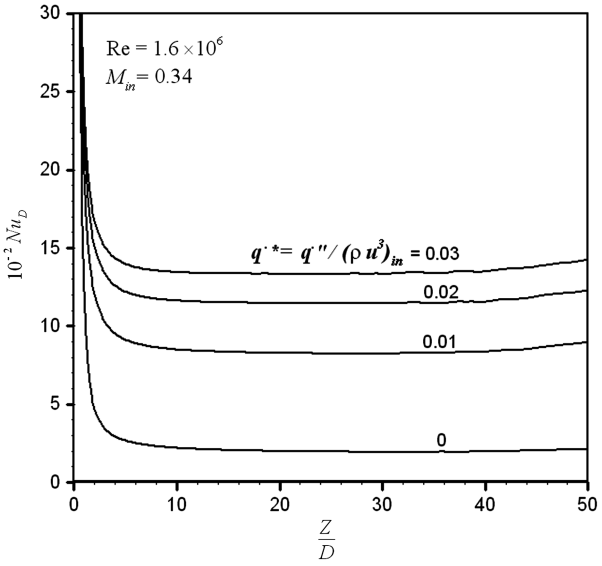


**Fig. 14 Nusselt number along the pipe for different wall heat fluxes.**

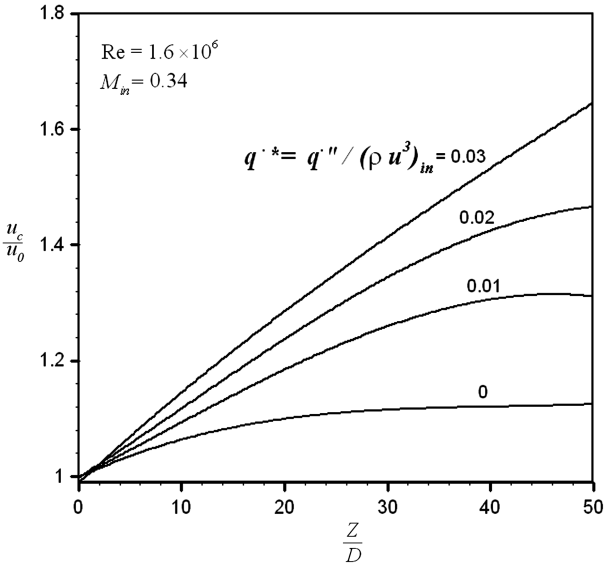


**Fig. 12 Fully developed centerline velocity along the pipe for different heat fluxes.**

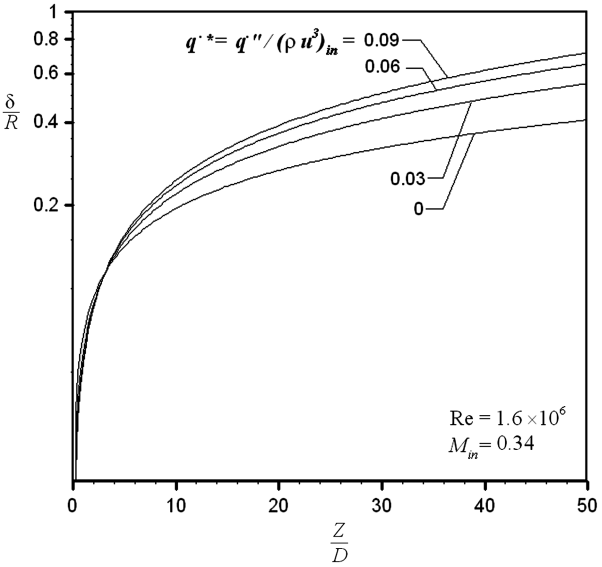


**Fig. 15 Boundary-layer development along the pipe for different wall heat fluxes.**

heat flux on the wall, of course, will result in more gas velocity and consequently more pressure drop. Note that a wall heat flux of $q^* = 0.03$ can increase the pressure drop up to 12%.

## VI. Conclusions

A two-dimensional turbulent compressible airflow at high pressure is numerically studied with wall heat flux. The objective of this research is to study the process of the pressure drop, Nusselt number, and friction factor in the developing as well as developed region of a turbulent compressible pipe flow. A computer code is developed using a finite-element-based finite volume method for unstructured grids. Generation of the computational grid nodes is automated as a part of the code. Turbulence modeling is based on the $\kappa$-$\varepsilon$ model using a two-layer technique near the wall.

The results show significant differences between incompressible and compressible flow. The shear stress in fully developed flow is nearly constant from the centerline up to 75% of the pipe radius and then increases sharply next to the wall, whereas this behavior is linear for the incompressible flow across the pipe from the centerline to the wall. In addition, the ratio of the compressible turbulent viscosity to the molecular viscosity is less than 1, whereas it is much larger than 1 for the incompressible flow, and this in itself is a significant difference between internal compressible and incompressible flow. The results also indicate that the friction coefficient decreases with the wall heat flux and that the flow is fully developed for $Z/D > 50$, whereas the Nusselt number increases with heat flux and the flow is thermally fully developed for $Z/D > 10$. In addition, the heat flux accelerates the developing compressible flow and causes the entrance length to decrease, unlike the incompressible flow.

## References


[1] Oosthuizen, P. H., and Carscallen, W. E., *Compressible Fluid Flow*, McGraw–Hill, New York, 1997.

[2] Cebeci, T., and Smith, A. M. O., *Analysis of Turbulent Boundary Layers*, Academic Press, New York, 1974.

[3] Schreier, S., *Compressible Flow*, Wiley, New York, 1982.

[4] Anderson, J. D., *Hypersonic and High-Temperature Gas Dynamics*, McGraw–Hill, New York, 1989.

[5] Kafoussias, N., Karabis, A., and Xenos, M., "Numerical Study of Two Dimensional Laminar Boundary Layer Compressible Flow with Pressure Gradient and Heat and Mass Transfer," *International Journal of Engineering Science*, Vol. 37, No. 14, 1999, pp. 1795–1812. doi:10.1016/S0020-7225(99)00002-6

[6] Toplak, E., "Gasströmung Durch Rohre Unter Berücksichtigung der Rohrreibung und Eines Wärmeaustauschs mit der Umbegung bei Konstanter Heizfächenbelastung," *Forschung im Ingenieurwesen / Verein Deutscher Ingenieure*, Vol. 40, No. 4, 1974, pp. 120–125. doi:10.1007/BF02561315

[7] Landram, C. S., "One-Dimensional Steady Compressible Flow with Friction Factor and Uniform Heat Flux at the Wall Specified," Lawrence Livermore National Lab., TR UCRL-ID-128670, Livermore, CA, 27 Oct. 1997.

[8] Ceylan, K., and Kelbaliyev, G., "The Roughness Effects on Friction and Heat Transfer in the Fully Developed Turbulent Flow in Pipes," *Applied Thermal Engineering*, Vol. 23, No. 5, 2003, pp. 557–570. doi:10.1016/S1359-4311(02)00225-9

[9] Browne, L. W. B., and Dinkelacker, A., "Turbulent Pipe Flow: Pressures and Velocities," *Fluid Dynamics Research*, Vol. 15, No. 3, 1995, pp. 177–204. doi:10.1016/0169-5983(94)00038-2

[10] De Chant, L. J., "An Analytical Skin Friction and Heat Transfer Model for Compressible, Turbulent, Internal Flows," *International Journal of Heat and Fluid Flow*, Vol. 19, No. 6, 1998, pp. 623–628. doi:10.1016/S0142-727X(98)10010-3

[11] Mohanty, A. K., and Asthana, S. B. L., "Compressible Laminar Flow in the Inlet Region of a Smooth Circular Pipe," *Journal of Physics D: Applied Physics*, Vol. 13, No. 11, 1980, pp. 2021–2030. doi:10.1088/0022-3727/13/11/013

[12] Xu, X., Lee, J. S., and Pletcher, R. H., "A Compressible Finite Volume Formulation for Large Eddy Simulation of Turbulent Pipe Flows at Low Mach Number in Cartesian Coordinates," *Journal of Computational Physics*, Vol. 203, No. 1, 2005, pp. 22–48. doi:10.1016/j.jcp.2004.08.005

[13] Lin, T. F., Hawks, K. H., and Leidenfrost, W., "Unsteady Thermal Entrance Heat Transfer in Laminar Pipe Flows with Step Change in Ambient Temperature," *Wärme- und Stoffübertragung*, Vol. 17, No. 3, 1983, pp. 125–132.

[14] Wilcox, D. C., "Dilatation-Dissipation Corrections for Advanced Turbulence Models," *AIAA Journal*, Vol. 30, No. 11, 1992, pp. 2639–2646. doi:10.2514/3.11279

[15] Wolfstein, M., "The Velocity and Temperature Distribution of One-Dimensional Flow with Turbulence Augmentation and Pressure Gradient," *International Journal of Heat and Mass Transfer*, Vol. 12, No. 3, 1969, pp. 301–318. doi:10.1016/0017-9310(69)90012-X

[16] Roe, P. L., "Characteristic-based Schemes for the Euler Equations," *Annual Review of Fluid Mechanics*, Vol. 18, 1986, pp. 337–365. doi:10.1146/annurev.fl.18.010186.002005

[17] Steger, J., and Warming, R. F., "Flux Vector Splitting for the Inviscid Gas Dynamic with Applications to Finite Difference Methods," *Journal of Computational Physics*, Vol. 40, No. 2, 1983, pp. 263–293.

[18] Wang, C. R., Towne, C. E., Hippensteele, S. A., and Poinsatte, P. E., "Heat Transfer Computations of Internal Duct Flows with Combined Hydraulic and Thermal Developing Length," NASA TM-107450, May 1997.

[19] Ward-Smith, A. J., *Internal Fluid Flow*, Clarendon Press, Oxford, 1980, pp. 247–249.

[20] Haaland, S., "Simple and Explicit Formulas for the Friction Factor in Turbulent Pipe Flow," *Journal of Fluids Engineering*, Vol. 105, No. 3, 1983, pp. 89–90.

[21] Gnielinski, V., "New Equations for Heat and Mass Transfer in Turbulent Pipe and Channel Flow," *International Chemical Engineering*, Vol. 16, No. 2, 1976, pp. 359–368.

[22] Eggels, J. G. M., Unger, F., Weiss, M. H., Westerweel, J., Adrian, R. J., Friedrich, R., and Nieuwstadt, F. T. M., "Fully Developed Turbulent Pipe Flow: A Comparison between Direct Numerical Simulation and Experiment," *Journal of Fluid Mechanics*, Vol. 268, No. -1, 1994, pp. 175–209. doi:10.1017/S002211209400131X

[23] Imao, S., and Itoh, M., "Turbulent Characteristics of the Flow in an Axially Rotating Pipe," *International Journal of Heat and Fluid Flow*, Vol. 17, No. 5, 1996, pp. 444–451. doi:10.1016/0142-727X(96)00057-4